Title

Spatial distribution of crystalline corrosion products formed during corrosion of stainless steel in concrete

Authors

Serdar, Marijana
Meral, Cagla
Kunz, Martin
et al.

Publication Date

2015-05-01

DOI

10.1016/j.cemconres.2015.02.004

Peer reviewed

Cement and Concrete Research 71 (2015) 93–105

Contents lists available at ScienceDirect

Cement and Concrete Research

journal homepage: http://ees.elsevier.com/CEMCON/default.asp

Spatial distribution of crystalline corrosion products formed during corrosion of stainless steel in concrete

Marijana Serdar [a], Cagla Meral [b], Martin Kunz [c], Dubravka Bjegovic [a], Hans-Rudolf Wenk [d], Paulo J.M. Monteiro [e,*]

[a] Department of Materials, Faculty of Civil Engineering, University of Zagreb, 10000 Zagreb, Croatia
[b] Middle East Technical University, Department of Civil Engineering, Ankara, Turkey
[c] Lawrence Berkeley National Laboratory, 1 Cyclotron Road, Berkeley, CA 94720, United States
[d] Department of Earth and Planetary Science, University of California, Berkeley, CA 94720, United States
[e] Department of Civil and Environmental Engineering, University of California, Berkeley, CA 94720, United States

ARTICLE INFO

Article history:
Received 6 October 2013
Accepted 6 February 2015
Available online 19 February 2015

Keywords:
Backscattered Electron Imaging (B)
X-ray micro-diffraction (B)
Corrosion (C)
Concrete (E)
Stainless steel

ABSTRACT

The mineralogy and spatial distribution of nano-crystalline corrosion products that form in the steel/concrete interface were characterized using synchrotron X-ray micro-diffraction (μ-XRD). Two types of low-nickel high-chromium reinforcing steels embedded into mortar and exposed to NaCl solution were investigated. Corrosion in the samples was confirmed by electrochemical impedance spectroscopy (EIS). μ-XRD revealed that goethite (α-FeOOH) and akaganeite (β-FeOOH) are the main iron oxide–hydroxides formed during the chloride-induced corrosion of stainless steel in concrete. Goethite is formed closer to the surface of the steel due to the presence of chromium in the steel, while akaganeite is formed further away from the surface due to the presence of chloride ions. Detailed microstructural analysis is shown and discussed on one sample of each type of steel.

1. Introduction

In non-carbonated and chloride-free concrete, embedded steel reinforcement is protected from corrosion by a protective oxide film that forms on the steel surface. However, in less-than-ideal conditions this is not the case. A decrease in concrete alkalinity may cause failure of the stable chemical environment around the steel reinforcement. Also, a rise of the concentration of chloride ions above a threshold value in the vicinity of steel reinforcement may lead to a localised breakage of the passive layer [1]. Once the passive layer is dissolved or broken corrosion is initiated, and a second stage of corrosion starts, i.e., the corrosion propagation period, during which corrosion products are formed on the surface of the steel [2]. These corrosion products are mainly iron oxides and iron oxide–hydroxides, which have a larger specific volume than pure iron. The resulting volume expansion during the build-up of corrosion products creates radial pressure at the steel/concrete interface, leading to concrete cracking and delaminating, and eventually structural instability and failure [3]. Models that consider the radial pressure at the interface between the cement matrix and reinforcing steel – which leads to tensile stresses greater than the concrete tensile strength and thus cracking – take into account properties of concrete (e.g., residual compressive and tensile strength, stiffness, modulus of elasticity) and properties of corrosion products (e.g., rate of formation, depth of penetration into the matrix, volume, and morphology of corrosion products) [4–11]. Due to the critical role that corrosion products play in understanding the propagation of corrosion, cracking and the eventual failure of concrete, several comprehensive studies were performed to characterize the different iron oxides and iron oxide–hydroxides that form during corrosion of carbon steel reinforcement [13–17] and weathering steels [12,18,19]. However, previous studies investigating corrosion products formed on carbon steel reinforcement in concrete [13–16] have not reported the spatial distribution of the crystalline phases in the corrosion products near the steel-cement matrix interface. This information is critical to better understand the corrosion process, the formation of corrosion products, and the generation of stress on the interface leading to concrete cracking.

Nowadays, stainless steels are widely utilized as reinforcement instead of carbon steel, especially when durability due to aggressive environment exposure is a concern. Because of rising nickel prices, however, new types of corrosion resistant steels with lower percentages of alloying elements have been developed, e.g., low-nickel, high-chromium corrosion-resistant steels, which can be a cost-effective corrosion resistant alternative to highly alloyed stainless steels. So far, published research on these types of steel as concrete reinforcement has focused on the corrosion initiation phase, mainly on the characterization of the passive film, and on the critical conditions for the onset of corrosion [20–24]. Long-term research of

* Corresponding author. Tel.: +1 510 643 8251; fax: +1 510 643 8928.
E-mail address: monteiro@ce.berkeley.edu (P.J.M. Monteiro).

http://dx.doi.org/10.1016/j.cemconres.2015.02.004
0008-8846/

corrosion behaviour of these steels in concrete is very scarce, especially those aiming at evaluating the real-time propagation of corrosion and the formation of corrosion products. Until now, research on laboratory samples and long-term exposure of real concrete reinforced structures to marine environments have shown that, besides longer initiation periods, these steels have a prolonged propagation period (i.e., more time is needed to achieve a certain level of corrosion activity) [25,26]. The available literature on corrosion products formed under the influence of alloying elements concentrates mainly on synthesized iron oxide–hydroxides, created and tested under laboratory-controlled conditions [12,27–31]. These studies have demonstrated that adding specific alloys influences the type of iron–hydroxide phases created during the corrosion process.

The present study aims at determining the type, morphology, and in-situ spatial distribution of the crystalline phases of corrosion products that form during natural (non-accelerated) corrosion of two types of low-Ni, high-chromium Cr corrosion resistant steel embedded in mortar. Reinforced mortar samples were exposed to an aggressive chloride solution for two years, during which their corrosion activity was confirmed by (1) monitoring the corrosion potential and (2) by analysing electrochemical impedance spectra (EIS) at the open circuit potential (E_{OC}). Next, corrosion products formed in the steel–cement matrix interface were analysed with synchrotron radiation to determine their type and distribution relative to the surface of the reinforcement. Using synchrotron-based X-ray micro-diffraction (μ-XRD), two-dimensional maps showing the distribution of crystalline phases with a high spatial resolution were obtained. Besides the μ-XRD used for identification of crystalline phases, X-ray micro-fluorescence (μ-XRF) was also used for elemental mapping to differentiate between corrosion products and the cement paste matrix, thus locating areas of interest (e.g., iron-rich or chromium-rich areas). Scanning Electron Microscopy (SEM) combined with Energy Dispersive Spectrometry (EDS) was used for imaging and to determine the chemical composition of recognized corrosion products.

2. Experimental program

2.1. Materials

Two types of low-Ni, high-Cr steel were studied. One of the steels had 10 wt.% Cr (UNS S41008, EN 1.4003) and the other 16 wt.% Cr (UNS S20430, EN 1.4597). Both steels had significantly lower Ni content compared to classical stainless steel (less than 2 wt.%, compared to typical alloyed stainless steel with 8 to 13 wt.%). Table 1 lists their chemical composition. Both tested steels are commercially available on the market as corrugated reinforcing steel, and both were embedded into the mortar as received from the manufacturer. The surface of the reinforcing steels was not additionally pre-treated, with an intention to simulate what would happen during real construction in the case of application of these steels as reinforcement. Production processes of both of the tested steels are protected by the producers. Based on the appearance of the surface of the steel, it could be assumed that 10% wt Cr steel was not pickled, while 16% steel was pickled in the production phase.

The mortar used to embed the steels was prepared using cement CEM I 42.5 (cement without mineral admixture, similar to ASTM cement Type I), with a 0.7 water-to-cement ratio. Crushed limestone with a maximum particle size of 4 mm was chosen as the aggregate. The mortar mix proportion was chosen so that the ratio between constituent materials (water, cement and aggregate) was identical to the concrete labelled C(0.7) according to European standard EN 1766: 2000. In this standard, the preparation of reference concrete is described, which is used to perform comparative tests for evaluating the influence of products and systems for repair and protection of reinforced concrete structures. Therefore, to evaluate the influence of corrosion resistant steel composition on the corrosion behaviour of reinforced concrete and to keep the concrete quality constant for both steel types, a similar mortar to that C(0.7) of known properties was prepared. Corrosion was not accelerated electrochemically; rather, it was allowed to initiate and propagate naturally. To obtain a significant amount of corrosion products in a reasonable time, a mortar with high water-to-cement ratio was used. It is assumed that a better quality concrete would not change the morphology or chemical composition of the corrosion products; however, it would prolong the time to onset of active corrosion, change the properties of the interfacial zone between steel and matrix, and influence the mobility of ions inside the cement matrix. However, since the aim of the paper is to compare two different types of steel in the same mortar mixture, it can be expected that this influence would be similar for both steel types.

The mortar was cured for 28 days in a humidity chamber, with controlled humidity (95% RH) and temperature (20 ± 2 °C). After 28 days, the compressive strength of the mortar was measured as 32.7 MPa. The mortar also showed a low resistance to chloride penetration (non-steady state chloride migration coefficient tested according to NT BUILD 492; measured as 2×10^{-11} m^2 s^{-1}).

2.2. Preparation of the samples

The 14 mm-diameter steel rebar from the selected two different steels were cut into 100 mm-long pieces, providing an approximate steel testing area of 45.5 cm^2 for each segment. A copper wire was welded to the top end of each segment for the electrical connection. The weld was protected with a polyester-based sealing material. This connection was necessary to monitor the corrosion potential and obtain impedance spectra of the steel during the two-year-long exposure of the samples to aggressive conditions that simulated a marine environment. The steel segments were placed into 40 mm-diameter and 140 mm-long plastic moulds and fresh mortar was then placed into the moulds embedding the steel. A special holder for moulds was prepared, consisting of 10 samples. The wire which was connected to the reinforcing steel for electrochemical testing was fixed on the bottom of the holder, to ensure that the steel will stay in the centre of the mould. Once the mortar was placed inside the mould, the mould holder with all samples was placed on a vibrating table to ensure full compaction of the samples. Samples were checked after demoulding, to ensure that there were no visible defects of the samples. Three replica samples were prepared as described and were cured in a humidity chamber for 28 days with controlled humidity (95% RH) and temperature (20 ± 2 °C) and were subsequently partially submerged into a 3.5 wt.% NaCl solution (0.6 mol dm^{-3}). A schematic sketch of the sample assembly is shown in Fig. 1(a). Oxygen penetration was expected to proceed from the upper part of the samples and chloride penetration from the submerged part of the specimen. Based on the corrosion potential

Table 1
Elemental composition of the investigated steels.

Steel type	Elemental composition, wt.%									
	C	Si	Mn	S	N	Cr	Cu	Mo	Ni	Fe
10% Cr steel	≤0.03	≤1.00	≤1.50	≤0.015	≤0.03	10.50	–	–	0.30	*Bal.*
16% Cr steel	≤0.10	≤2.00	7.50	≤0.003	0.15	16.00	2.00	≤1.00	<2.00	*Bal.*

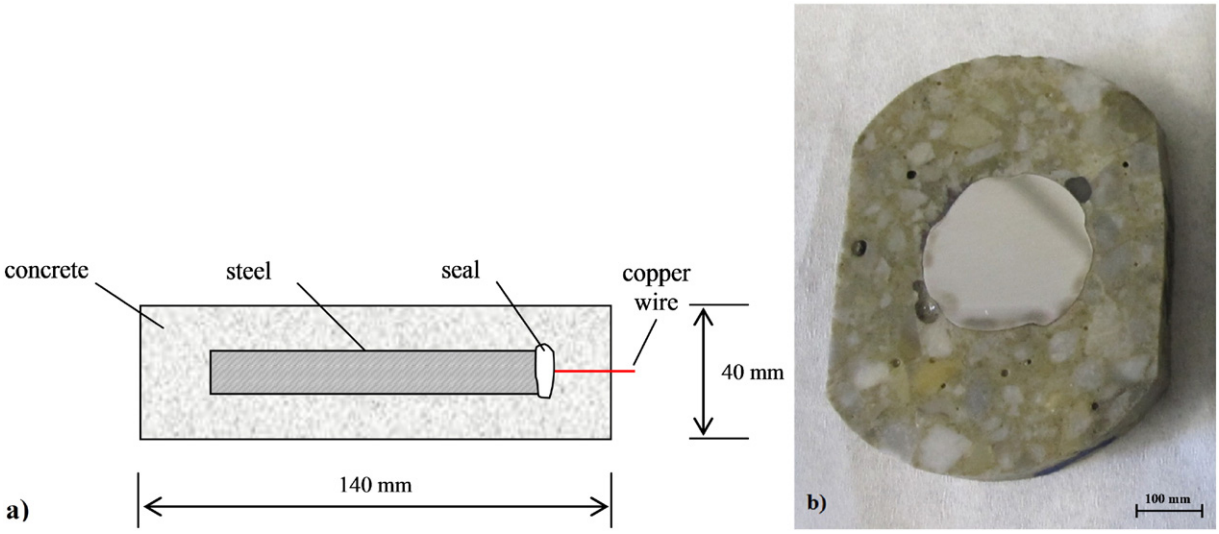

Fig. 1. (a) Schematic of the cast samples; (b) sample after sawing, grinding and polishing.

measurement and impedance spectra data representative specimens were chosen for detailed microstructural analysis, and it is expected that these specimens can be representatives of the group. After two years of exposure, this representative specimen of each type of steel was cut into 1-cm-thick slices. To ensure that all voids in the matrix as well as the interface were filled with epoxy, one side of the slice was vacuum impregnated with low-viscosity epoxy resin. Next, the surfaces were carefully polished on a grinding plate with 20, 9, and 3 μm Al_2O_3 powder. The final polish was completed using an oil-based paste with 0.25 μm diamond abrasives. During the grinding and polishing, kerosene was used instead of water to avoid any further reaction in the specimen. To prevent charging, a 20 nm-thick coating of carbon was applied on the specimens before conducting the SEM investigations. Fig. 1(b) shows the specimens as used in the microscopic investigations.

It has to be noted that, even though samples were impregnated with epoxy and kerosene was used during grinding and polishing, the process of cutting and grinding the sample may have induced additional cracks in the sample and some short exposure to oxygen may have changed the micro-structure of the products. This surely is one of the main drawbacks in using methods that need detailed and destructive sample preparation when investigating corrosion of reinforcing steel in concrete. However, high spatial resolution and the possibility of phase identification and mapping is unique to this method, which is why it was used for this specific purpose.

2.3. Monitoring corrosion potential and impedance spectra

During the exposure, the corrosion activity of reinforcing steels was monitored by measuring open-circuit potential (E_{OC}) and by performing electrochemical impedance spectroscopy (EIS). A standard three-electrode system with a titanium mesh as a counter and a saturated calomel electrode (SCE) as a reference electrode was used. All potentials reported refer to the SCE. EIS measurements were performed in the frequency range between 100 kHz and 0.1 mHz with the ac perturbation ± 10 mV. The impedance spectra fitting was carried out using the commercial software ZView.

2.4. Scanning Electron Microscope (SEM) and Energy Dispersive Spectrometry (EDS)

The SEM and EDS investigations were performed at the Department of Earth and Planetary Science at the University of California, Berkeley. The SEM was operated in backscatter mode, at an accelerating voltage of 15 kV for imaging and 25 kV for elemental analysis of the corrosion products. For imaging and microstructure investigations, magnifications in the range of 60 to 1000× were used with the probe current ranging between 500 pA and 2 nA. The EDS point analysis and multi-element mapping were employed at specific positions on the sample to obtain the elemental analysis of corrosion products at the steel/cement matrix interface. Element mapping was performed at high energy (25 kV) and high probe current (around 3.0 nA) to optimize the counting statistics.

2.5. Micro-X-ray Diffraction (μ-XRD) and micro-X-ray Fluorescence (μ-XRF)

Synchrotron μ-XRD measurements, carried out on beamline 12.3.2 at the Advanced Light Source (ALS), Lawrence Berkeley National Laboratory [32,33], were used to characterize the corrosion products and to identify their spatial distribution. Beamline 12.3.2 offers the ability to operate with polychromatic (5–22 keV) or monochromatic beams [34,35]. In the case of the 10 wt.% Cr steel, a 450 μm × 550 μm area scan was collected, with a 20 μm step size in the *x*-direction and a 50 μm step size in the *y*-direction. In the case of the 16 wt.% Cr steel, two 500 μm × 400 μm area scans were collected, with a 20 μm scan step in the *x*-direction and a 100 μm scan step in the *y*-direction. A diffraction pattern was collected at each step using the Pilatus 1 M detector (169 × 179 mm with 981 × 1043 pixels of 0.172 μm edge length). The scans were done in reflection mode, using a monochromatic beam (energy 10 keV, λ = 1.23986 Å) while collecting diffraction data. The detector was positioned at an angle 2θ of 47° with respect to the incident beam. The angle of incident beam relative to the sample surface was 5°. The sample to detector distance was 145.93 mm. More details on the general experimental set-up for beamline 12.3.2 can be found in Kunz et al. [33].

Although beamline 12.3.2 is optimized for μ-XRD, it also allows collection of fluorescence signals through a VORTEX Si-drift detector that can be used to locate areas enriched with elements heavier than Ca ($Z > 20$). In the present study, μ-XRF was employed for the localization of elements of interest; this was done to differentiate the area of corrosion products from the cement matrix and pure steel. In this way, μ-XRF maps helped to correlate sample positions during the μ-XRD experiment with regions of interest identified in backscattered SEM images.

3. Results and discussion

3.1. Corrosion activity

Fig. 2 shows representative results of E_{OC} time dependence, obtained from parallel measurements performed on 3 identical samples for each of the steel embedded into mortar, during 24 months of exposure to 3.5 wt.% NaCl solution. It can be observed that for the entire exposure time the potential of the 16 wt.% Cr steel was more anodic than the potential of the 10 wt.% Cr steel. After 24 months of exposure both the potential of the 10 wt.% Cr steel and 16 wt.% Cr steel decreased compared to the values after one month of exposure, but the latter value was still significantly more anodic than the former. The change of E_{OC} towards more negative values can be considered as indicative of depassivation of steel and initiation of localized corrosion. In this study we focused on the time-dependence of the potential where a rapid decrease of the potential is interpreted as destabilization or breakdown of the passive film and initiation of pitting corrosion. This interpretation is further supported by EIS results. EIS spectra for 10 wt.% Cr steel and 16 wt.% Cr steel after one month of exposure are presented in Fig. 3. After one month of exposure, a passive state is assumed for both steels. An electrical circuit (EC) was used to describe the behaviour of the tested steels and is shown on Fig. 3(a). In the electrical circuit, constant-phase elements (CPE) were used instead of the pure capacitance to take into account the inhomogeneity present at the reinforcement/pore solution interface [36]. The impedance of a CPE is defined as $Z_{CPE} = [CPE(j\omega)^n]^{-1}$ [37]. During the fitting process, values of n were smaller than 1 for both samples, indicating that the behaviour of the system is not purely capacitive and that CPE should be used. Furthermore, this analysis of the proposed electrical circuit yielded fitted data with the error below 10% for all parameters. The accuracy of fitting is illustrated in Fig. 3(a) and (b), with experimental values presented as symbols and fitted values as lines. The physical meaning of the components in the proposed circuit during the passive state is the following: resistance R_{mortar} can be related to the resistance of testing solution and mortar. The first time constant parameters (resistance R_1 and constant phase element CPE_1) appearing at the intermediate frequencies (between 10 Hz and 10^{-1} Hz) were attributed to the redox transformation which occurs on the outer region of the passive layer [23,24]. The second time constant parameters (resistance R_2 and constant-phase element CPE_2) appearing at the low frequencies (between 10^{-1} and 10^{-3} Hz) were attributed to the non-ideal interfacial capacitance of the steel surface and charge transfer resistance that reflects the corrosion resistance of the steel surface controlled by the properties of the passive film [22,24].

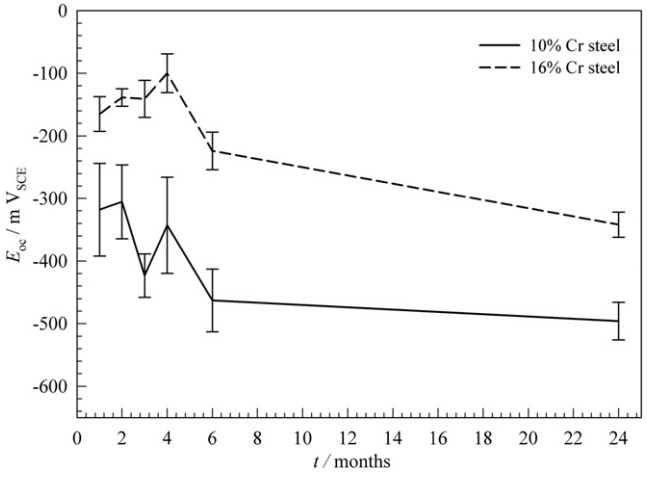

Fig. 2. Open circuit potential (E_{OC}) of tested steels embedded into concrete during 24 months of exposure to 3.5% NaCl solution.

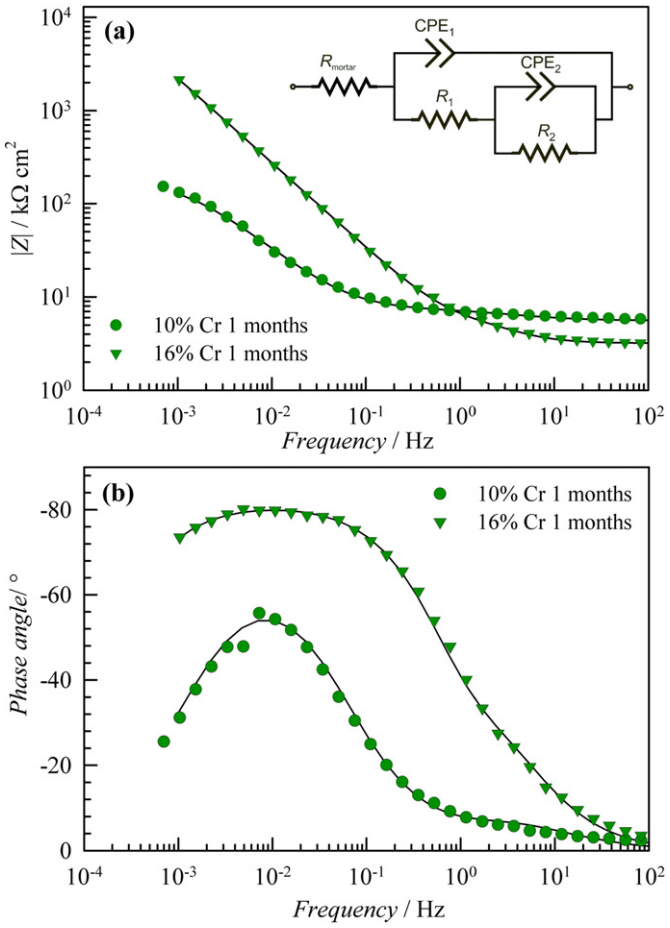

Fig. 3. (a) Bode and (b) Nyquist plots of impedance spectra for concrete sample reinforced with the 10 wt.% Cr steel and the 16 wt.% Cr steel after 1 month of exposure to 3.5 wt.% NaCl solution. Proposed EC used for fitting is shown in the upper corner; experimental values given as dots, fitted values displayed as lines.

Fig. 4 presents the impedance spectra after 24 months of exposure for 10 wt.% Cr steel and 16 wt.% Cr steel, respectively. An electrical circuit was used to describe the behaviour of the tested steels and is shown in Fig. 4(a). Constant-phase elements CPE instead of the pure capacitance were used for longer exposure times, based on the same rationale used in the shorter exposure period. Here, the first time constant parameters (resistance R_1 and constant phase element CPE_1) appearing at the intermediate frequencies (between 10 Hz and 10^{-2} Hz) were attributed to the layer of corrosion products formed at the reinforcing steel surface, while the second time constant parameters (resistance R_2 and constant-phase elements CPE_2) appearing at the low frequencies (between 10^{-2} Hz and 10^{-4} Hz) were attributed to the sum of processes appearing at the pitted and passive area [38]. The accuracy of fitting is illustrated in Fig. 4(a) and (b), with experimental values presented as symbols and fitted values as lines (obtained error below 10% for all parameters).

Table 2 shows the best-fit parameters obtained by fitting spectra measured after one month while Table 3 displays the respective values after 24 months of exposure for both types of steel. Values of resistance are expressed over a whole surface of exposed steel (steel testing area of 45.5 cm^2). The constant-phase element values, obtained by fitting the spectra to proposed EC, were used to calculate the capacitance values, using the equation developed by Farcas et al. [37]. The resistance of the mortar and electrolyte R_{mortar}, is similar for both steels, with values being slightly higher in the case of 10 wt.% Cr steel at the beginning of the exposure, but declining over time for both specimens. The variation of these resistances can be attributed to the poor quality of the mortar as

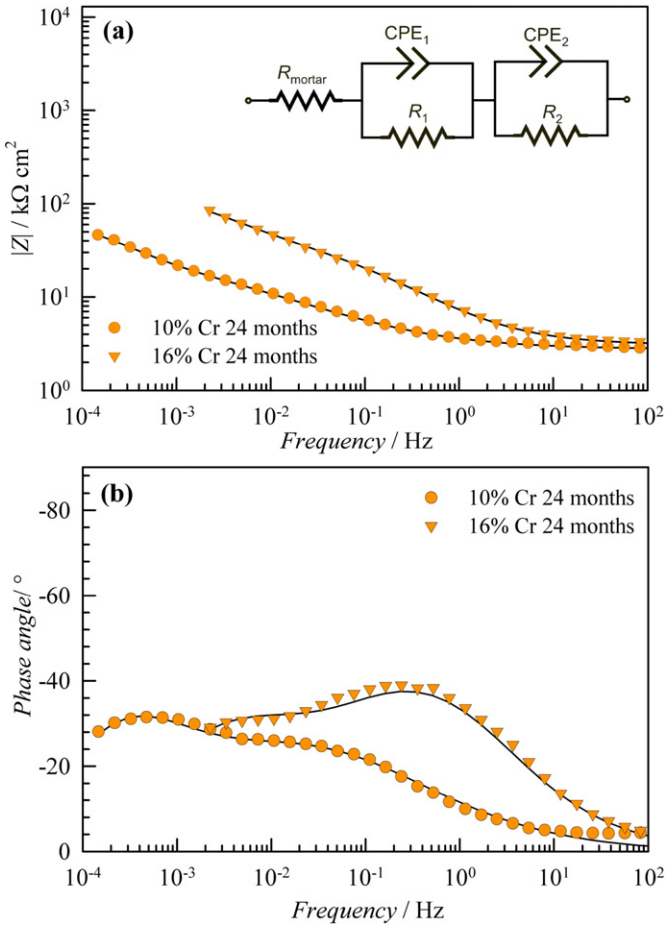

Fig. 4. (a) Bode and (b) Nyquist plots of impedance spectra for concrete sample reinforced with the 10 wt.% Cr steel and the 16 wt.% Cr steel after 24 months of exposure to 3.5 wt.% NaCl solution. Proposed EC used for fitting is shown in the upper corner; experimental values given as dots, fitted values displayed as lines.

water saturation and salt penetration inside the matrix caused the increase of the conductivity of the mortar. It is also possible that the variation in resistances is partly caused by varying distances between reference and working electrode due to the inability to perfectly replicate the electrochemical cell parameters during each testing. A comparison of resistances R_2 after one month of exposure, when both steels are passive, demonstrates that the charge transfer resistance of the passive film formed on 16 wt.% Cr steel is two orders of magnitude higher than of the 10 wt.% Cr steel (182.2 kΩ cm^2 compared to 14.1 MΩ cm^2). This significant difference can be attributed to the formation of a more stable Cr-rich passive film in the case of 16 wt.% Cr steel compared to the case of 10 wt.% Cr steel [21]. The resistances R_1 after one month of exposure have comparable values for both tested steels (several kΩ cm^2), supporting the attribution of this resistance to the redox transformation occurring on the surface of the oxide film formed on both types of steel.

After 24 months of exposure, the values of resistance R_1, ascribed to the layer of corrosion products, are higher in the case of 16 wt.% Cr steel than in the case of 10 wt.% Cr steel, 26.7 kΩ cm^2 and 16.7 kΩ cm^2, respectively. There was an even great discrepancy in the values of capacitance C_1 measured: 2 mF cm^{-2} for 10 wt.% Cr steel and 0.1 mF cm^{-2} for 16 wt.% Cr steel. Obtained values of capacitance were similar to the values obtained for carbon and corrosion-resistant steels during long-term exposure to aggressive environment [39].

A higher value of capacitance obtained for 10 wt.% Cr steel that for 16 wt.% steel indicates formation of a highly porous and heterogeneous layer of corrosion products. The resistance R_1 of 16 wt.% Cr steel is higher than that of 10 wt.% Cr steel, with significantly lower capacitance of this layer, indicating that the layer of corrosion products formed in the case of 16 wt.% Cr steel is more homogeneous and probably less porous. A comparison of the EIS parameters of the second time constant (R_2 and C_2) obtained for both types of steel after 24 months of exposure also revealed significantly higher resistance and significantly lower capacitance of the pitted and passive area of 16 wt.% Cr steel compared to 10 wt.% Cr steel. Therefore, even though the corrosion initiated and propagated for both steel specimens, the corrosion resistance of the 16 wt.% Cr steel was still significantly higher than that of the 10 wt.% Cr steel, even during the corrosion propagation period. Higher corrosion resistance of this steel during passivity is attributed to the composition of the passive film and is dependent on the chemical composition of the bulk material [20–22].

3.2. Phase distribution

Backscattered SEM (BSE) images (Figs. 5 and 6) were collected at low magnification (around 60×), which allowed for differentiation between phases in the sample (the steel is bright, the iron-rich interface with corrosion products are light grey, and the cement matrix is dark grey), and the correlation of the BSE image with μ-XRF maps. Fig. 5 shows a backscatter image of the 10 wt.% Cr steel and the mortar interface (a) together with the element mapping of (b) Ca, (c) Fe, and (d) Cr, obtained by μ-XRF of the same area. To allow comparison of the distribution of elements throughout the sample, the intensity of each element on a specific map-point was normalized relative to the maximum intensity of this element obtained on the mapped area, which explains the scale bar from 0 to 100 shown below the images. Note that the corrosion products are propagating from the steel surface through the cement matrix in a ~0.5 mm thick layer.

Fig. 6 shows the BSE image of the 16 wt.% Cr steel and the mortar interface (a) together with the element mapping of (b) Ca, (c) Fe, and (d) Cr, obtained by μ-XRF of the same area. On this steel, corrosion products are propagating from the steel surface through the cement matrix in a ~0.4 mm thick layer. The numbers on the BSE images and Fe and Cr map in Figs. 5 and 6 denote the spots where diffraction patterns were collected [shown below in Fig. 8(a) and (b)]. These specific locations were chosen depending on the relative amount of Fe and Cr, and their vicinity to the surface of the reinforcing steel. Positions 1 and 2 are close to the steel surface. Positions 3 and 4 are in the corrosion products/cement paste interface. Monochromatic diffraction measurements produced smooth Debye–Scherrer rings, revealing that corrosion products were nanocrystalline and that the monochromatic beam (2 × 20 μm) is appropriate for further characterization of these products. The obtained powder diffraction patterns covered a 2θ range of 8°–60°, corresponding to 1.2 < d < 8.5 Å. Fig. 7(a) shows an example of a diffraction pattern obtained with the instrument set-up described in Section 2.5. Integration along the azimuthal direction leads to a

Table 2
The best-fit parameters obtained by fitting spectra for 10 wt.% Cr steel and 16 wt.% Cr steel after 1 month of exposure.

Steel type	E_{ocv}, mV$_{SCE}$	R_{mortar}, kΩ cm^2	R_1, kΩ cm^2	C_1, μF cm^{-2}	n_1	R_2, kΩ cm^2	C_2, μF cm^{-2}	n_2
10 wt.% Cr	−0.318	5.6	2.3	26.8	0.75	182.2	516.5	0.85
16 wt.% Cr	−0.165	3.2	6.4	18.9	0.91	14,146.4	37.9	0.91

Table 3
The best-fit parameters obtained by fitting spectra for 10 wt.% Cr steel and 16 wt.% Cr steel after 24 months of exposure.

Steel type	E_{ocv}, mV_{SCE}	R_{mortar}, kΩ cm^2	R_1, kΩ cm^2	C_1, μF cm^{-2}	n_1	R_2, kΩ cm^2	C_2, μF cm^{-2}	n_2
10 wt.% Cr	−0.496	2.8	16.7	1980.0	0.51	55.5	24,683.1	0.80
16 wt.% Cr	−0.342	3.1	26.7	94.6	0.65	147.0	1145.9	0.70

regular one-dimensional intensity versus *d*-spacing or 2*θ* powder diffraction pattern. For phase identification, peak positions were compared against a crystal structure database, available as a part of the ALS in-house written μ-XRD analysis software (XMAS) [32]. Proper phase identification requires calibration of the instrumental geometry; in this case, this was accomplished through the diffraction patterns of Si and Al_2O_3.

Table 4 shows the main crystalline phases observed in the corrosion layer and the *d*-spacing and Miller indices of their high-intensity finger-print reflections that were used to identify them [40,41]. Other phases usually found as corrosion products display only high angle, low *d*-spacing reflections, which are difficult to use phase identification due to strong peak overlap at low *d*-spacings. Fig. 7(b) and

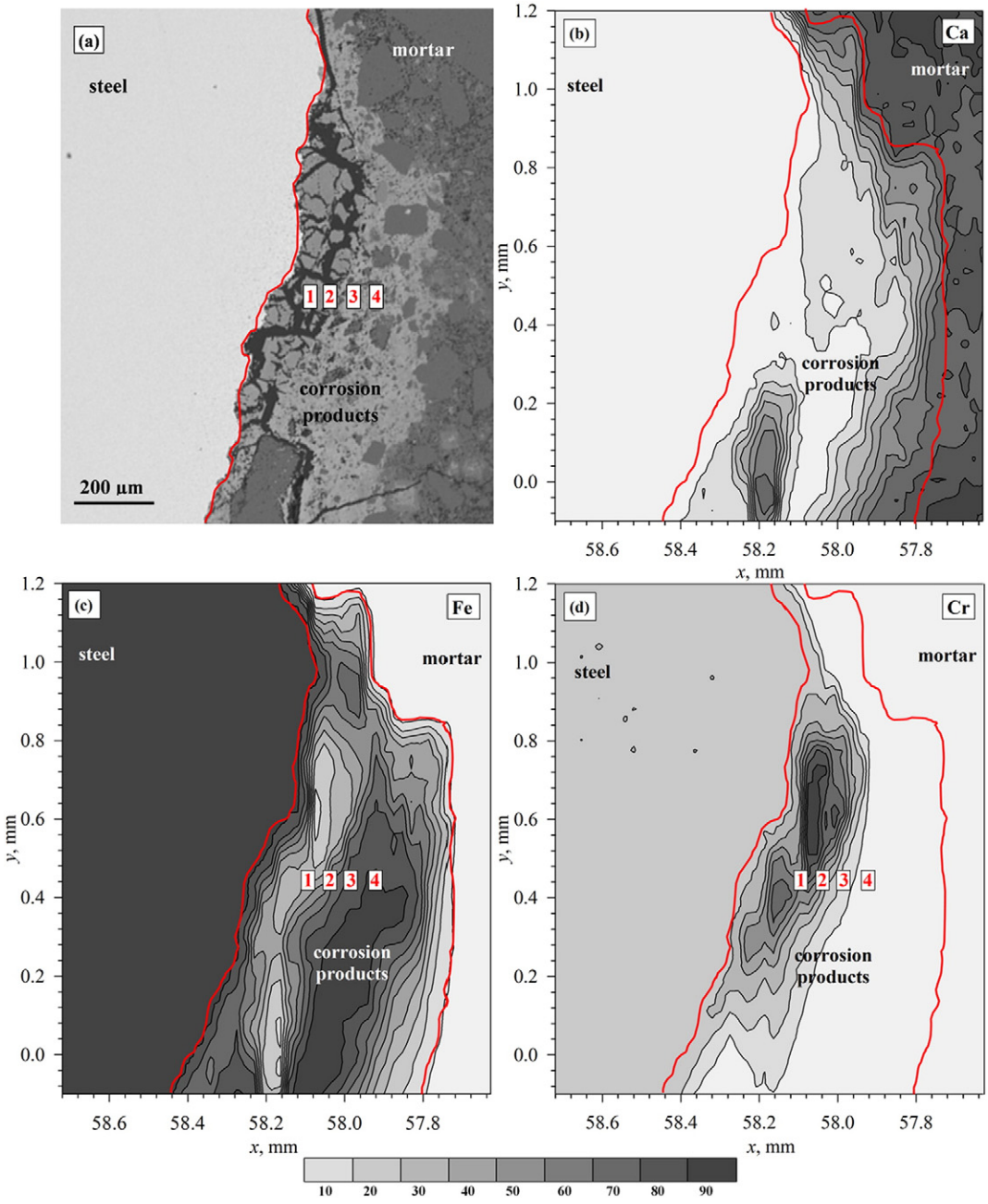

Fig. 5. (a) BSE image of the 10 wt.% Cr steel and mortar interface; and μ-XRF maps of the same area showing distributions and intensities of (b) calcium, (c) iron and (d) chromium. Numbers marked on the images represent the positions at which diffraction patterns presented in Fig. 8(a) were collected.

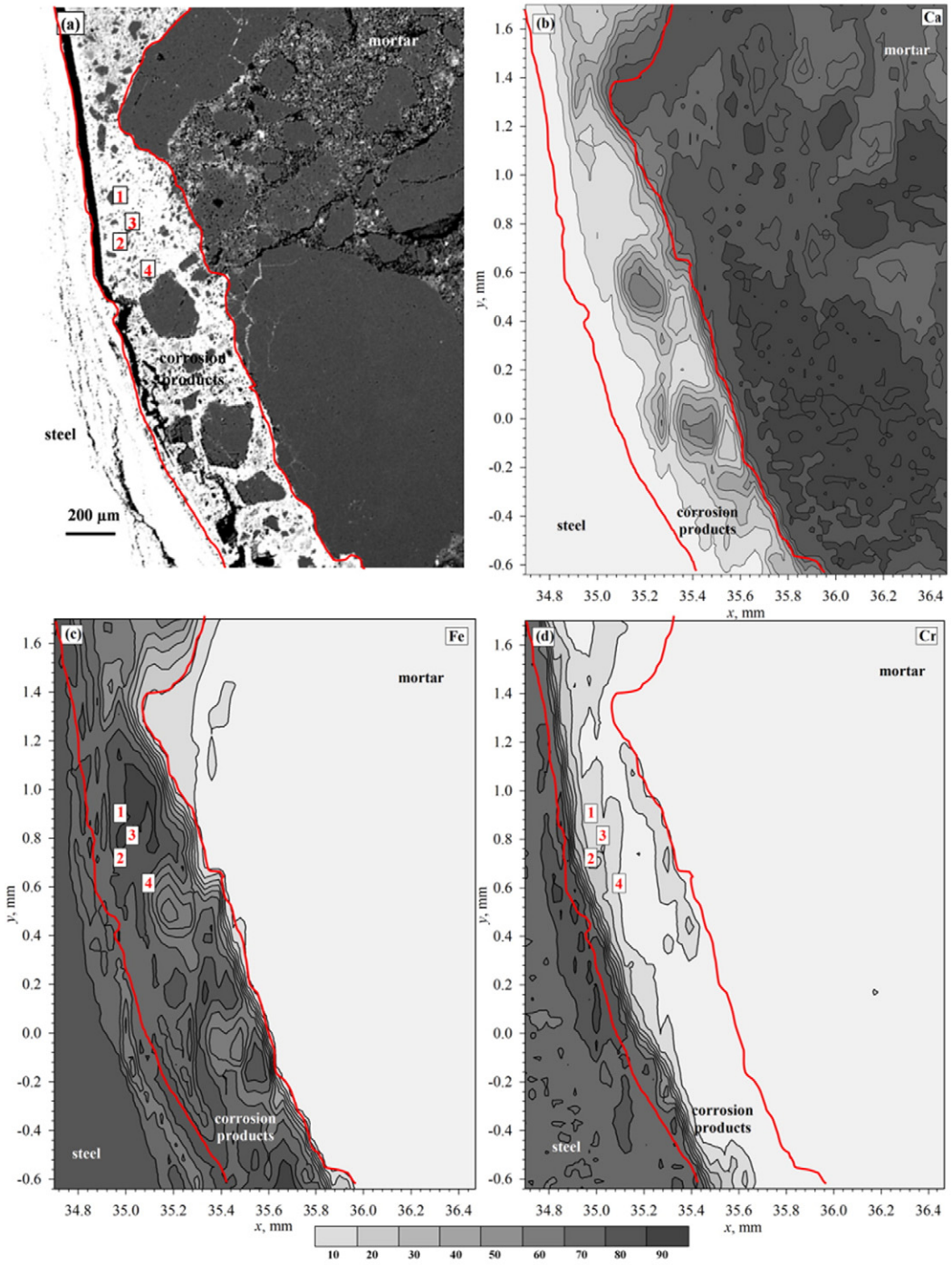

Fig. 6. (a) BSE image of the 16 wt.% Cr steel and mortar interface; and µ-XRF maps of the same area showing distributions and intensities of (b) calcium, (c) iron and (d) chromium. Numbers marked on the images indicate the positions at which XRD patterns in Fig. 8(b) were collected.

(c) shows identified diffraction rings for dolomite (aggregate) and akaganeite (corrosion products), respectively. In addition to the phases related to the corrosion products, the investigated samples were prepared from reinforced mortar, resulting in the observation of many phases related to the cement matrix and the aggregates. Dolomite and halite, due to their high crystallinity, showed the strongest peaks in the µ-XRD pattern and created strong individual spots, as opposed to the nanocrystalline corrosion products, which created smooth rings on the diffraction image. As hydration products and aggregates are not the subject of this research, their peaks were subtracted from diffraction patterns and are not displayed in the patterns shown in Fig. 8(a) and (b).

Fig. 8(a) and (b) shows µ-XRD patterns, which were obtained by integration over a 2θ range of 8°–60°, corresponding to $1.2 < d < 8.5$ Å, performed on a diffraction pattern collected on locations specified with numbers 1 to 4 in Figs. 5 and 6. The main phases were identified and their characteristic reflections are shown on the bottom of Fig. 8(a) and (b). The results of microdiffraction experiments presented in Fig. 8(a) and (b) show that akaganeite ($Fe^{3+}O(OH,Cl)$, also known as β-FeOOH) and goethite (α-FeOOH) are formed as

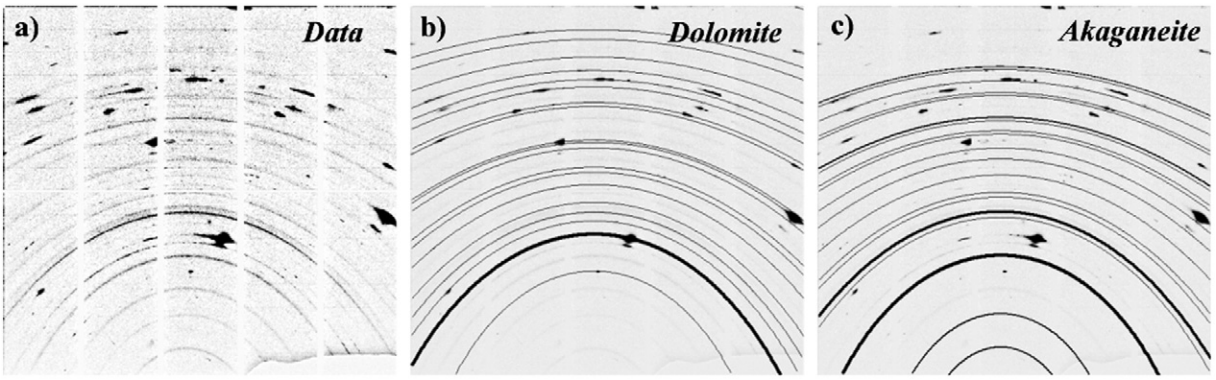

Fig. 7. (a) A representative monochromatic μ-XRD pattern (energy = 10 keV) showing partial Debye–Scherrer rings, (b) reflections of dolomite, and (c) reflections of akaganeite.

the main crystalline phases of the corrosion products of chromium-rich steel in concrete exposed to a marine environment.

Previous studies performed on synthesized iron oxide–hydroxides indicated that chromium influences the formation of goethite as a predominant crystalline phase compared to other iron oxide–hydroxides [18]. Akaganeite was found to be the main phase when corrosion occurred in marine environments [15–17,19]. Therefore, the influence of the steel composition and the environment around the steel in concrete explains why mainly these two iron oxide–hydroxides formed as corrosion product of chromium rich steel in concrete exposed to marine environment. In the case of the 10 wt.% Cr steel, chromite ($FeCr_2O_4$) is also identified at the edge of this reinforcing steel. Even though chromite and magnetite (Fe_3O_4) have similar diffraction patterns, the *d*-spacings of the phase observed here matched the ones of chromite better than magnetite. Also, EDS performed on the phase adjacent to the surface of the steel revealed high amounts of chromium, and the ratio between chromium and iron indicated chromite chemistry. Since chromite could potentially be a precipitate formed during production of this ferritic steel [42] and not a phase formed due to the corrosion process, it is not considered further.

Besides these phases, no other crystalline phases were found in any significant amount. In particular, the diffraction patterns suggest an absence of Cr or Ni oxide–hydroxides. This is attributed to the fact that other alloying metals are present in much lower amounts compared to iron. Compared to chromium, iron dissolves more readily and forms less stable compounds with oxides and hydroxides. These less stable compounds react more easily with chloride ions to form a soluble complex [3], which then precipitates in the pore solution away from the surface of the steel. This explains why iron-rich areas are found further away from the steel surface, while chromium-rich areas outside the steel are found only in a thin layer in immediate vicinity of the steel surface. Furthermore, the diffraction pattern shown in Fig. 8(a) and (b) seem to suggest that akaganeite and goethite grow by different mechanisms, depending on their proximity to the steel surface and the amount of Cr and Fe available. In the case of 10 wt.% Cr steel, akaganeite peaks were found closer to the steel surface, but they tended to be weaker and broader. With further distance from the steel surface, akaganeite peaks increased in intensity and became sharper, indicating a higher crystallinity and larger grain size. In the case of 16 wt.% Cr steel, mostly goethite is found in those areas closer to the surface of the steel; its peaks have high intensities and are sharp, indicating that goethite is in a well-crystallized phase in the area around the surface of this steel. In contrast, further away from the surface of the steel, goethite peaks become weaker and broader and akaganeite peaks more intense and sharper.

To further investigate the distribution of these two phases, two-dimensional phase distribution maps [shown In Figs. 9 and 10] were extracted from the diffraction area scans by integrating the intensity over a single finger-print diffraction ring [as opposed to the patterns shown in Fig. 8(a) and (b), which were obtained by integration over the full range of 2θ measured]. This was done using the (101) reflection at *d*-spacing 4.20 Å for goethite [40] and (512) reflection at *d*-spacing 1.63 Å for akaganeite [41]. Fig. 9 shows detailed investigation of an area of interest, performed using μ-XRF and μ-XRD on the 10 wt.% Cr steel reinforced mortar sample. The area of interest is chosen based on the μ-XRF maps (Fig. 5). The elemental maps for (a) Fe, (b) Cr, and (c) Ca, obtained through μ-XRF measurements are given on the left-hand side diagrams (with their scale bar), while corresponding intensity maps showing distribution of (d) chromite ($FeCr_2O_4$), (e) akaganeite (β-FeOOH), and (f) goethite (α-FeOOH), obtained through μ-XRD measurement, are given on the right-hand side diagrams. Fig. 10 shows detailed investigation of the area of interest performed using μ-XRF and μ-XRD on the 16 wt.% Cr steel reinforced mortar sample, which was chosen based on the μ-XRF maps, presented in Fig. 6.

The elemental maps for (a) Fe and (b) Cr obtained through μ-XRF measurements are given on the left-hand side diagrams (with their scale bar), while the corresponding intensity maps, showing distribution of (c) akaganeite and (d) goethite, obtained through μ-XRD measurement, are given on the right-hand side diagrams. As shown in Figs. 9 and 10, a layer of goethite is observed next to the steel surface, which is followed by layers of akaganeite. Previous studies have demonstrated that large amounts of both dissolved iron species and high chloride concentrations are necessary for the formation of akaganeite [27, 43]. In the investigated samples with embedded steels, it is possible that a large amount of dissolved iron and chloride ions could accumulate in the steel/cement mortar interface, thereby creating favourable conditions for akaganeite formation. The micro-diffraction experiments reported here show that the layer of goethite and the layer of akaganeite are negatively correlated, i.e., locations with higher amount of goethite have lower amounts of akaganeite, and vice versa.

Further investigation of the corrosion products formed in the steel/concrete interface was conducted examined using SEM and EDS. During the microscopic investigation of the 10 wt.% Cr steel interface, needle-like crystals were found in voids and cracks close to

Table 4
Main phases identified, three reflections used for their identification, Miller indices of planes producing reflections and their *d* spacing.

Type		Relative intensities *I*, *hkl*, *d*-spacing (Å)		
Chromite	$Fe_2(CrO_4)_3$	100, 311, 2.53	40, 440, 1.48	34, 220, 2.96
Goethite	α-FeOOH	100, 101, 4.20	72, 111, 2.44	45, 301, 2.69
Akaganeite	β-FeOOH	100, −101, 7.48	89, −103, 3.33	46, 200, 5.30
Halite	NaCl	100, 200, 2.83	66, 220, 1.99	22, 311, 1.63

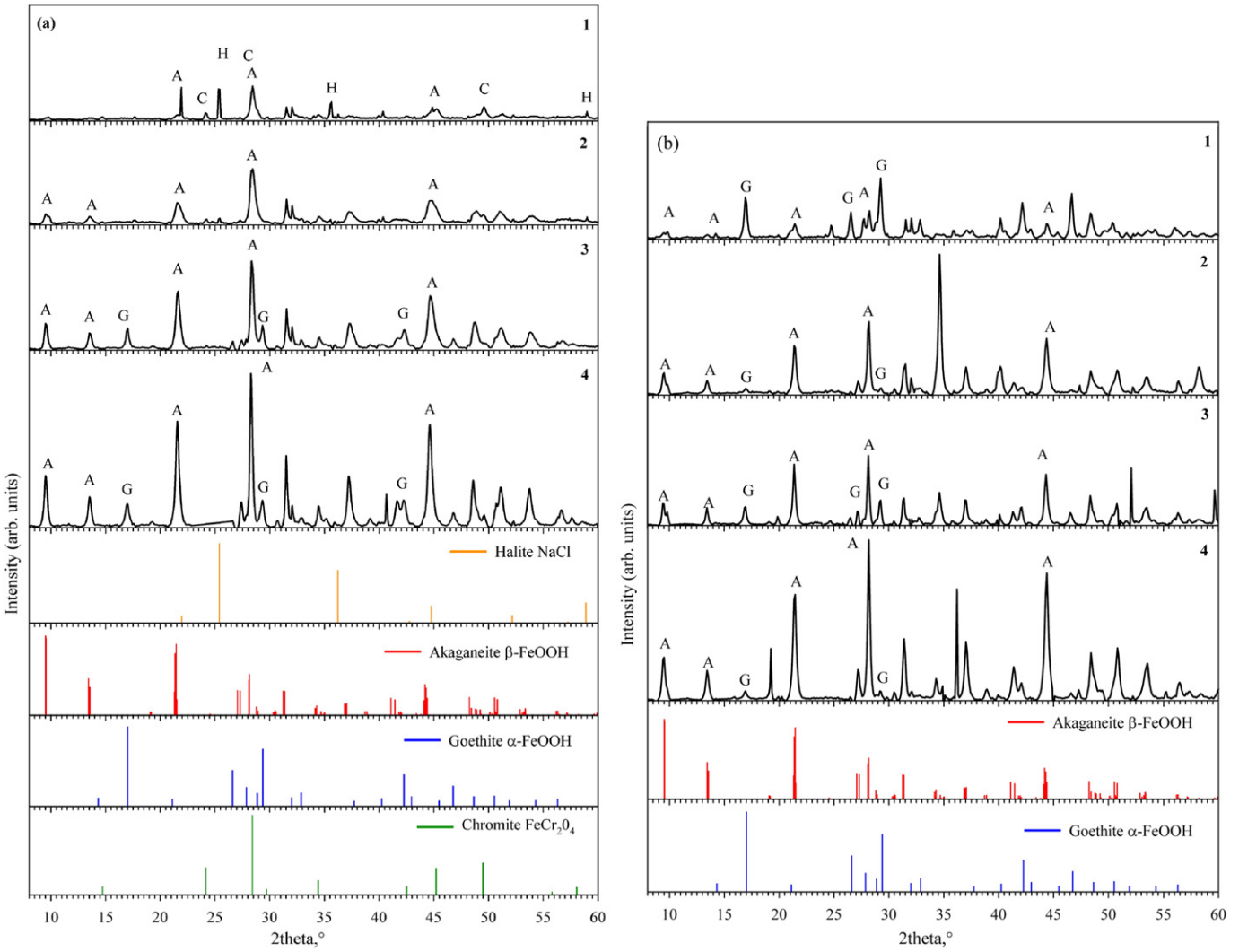

Fig. 8. Radial integration of the collected μ-XRD data for positions indicated on (a) Fig. 4, 10 wt.% Cr steel and (b) Fig. 5, 16 wt.% Cr steel. The major peaks of the identified phases are shown in the bottom of the plots where A — akaganeite (β-FeOOH), G — goethite (α-FeOOH), C — chromite ($FeCr_2O_4$), and H — halite (NaCl).

the surface of the steel, as shown in Fig. 11. These typical needle-like crystals are usually identified as akaganeite crystals due to their specific morphology and the significant amount of chloride in their composition [13]. This is in agreement with the μ-XRD results [Fig. 8(a)], which demonstrated that in the case of 10 wt.% Cr steel, akaganeite is found close to the surface of the steel. In the case of 16 wt.% Cr steel, no needle-like crystals were found close to the surface of the steel; rather these needle-like crystals formed further away of the surface in voids. They were usually found surrounded by platy-like crystals that did not have chlorides in their chemical composition. This is also in agreement with μ-XRD results [Fig. 8(b)], which showed that goethite had formed closer to the surface and was then followed by layers of akaganeite. An image of these groups of crystals is given in Fig. 12.

Besides BSE images of needle-like and plate-like crystals formed around a void, Fig. 12 shows iron and chromium distribution maps of the crystals obtained by EDS. The maps show that a certain amount of chromium is present in corrosion products that formed during corrosion of 16 wt.% Cr steel. Previous research performed on synthesized particles of different iron oxide–hydroxide has shown that cations such as Cr^{3+}, Cu^{2+}, Mn^{2+}, and Al^{3+} can substitute for iron in goethite, akaganeite, lepidocrocite, or magnetite [18,28–31]. Cook et al. [18] used Mössbauer and Raman spectrometry to characterize corrosion products that formed on weathering steel in natural environments, demonstrating that a layer of nano-sized chromium substituted goethite crystals formed close to the steel surface. They also prepared synthesized particles of goethite doped with Cr to show that incorporation of Cr changes the mean crystal size. Morales et al. [28] used transmission electron microscopy and Mössbauer spectroscopy on synthesized goethite samples and, based on the hyperfine parameters of the tested samples, demonstrated that most of the particles present in pure goethite are larger than 13 nm; in Cr-substituted goethite, however, most of the particles ranged between 8 and 13 nm. Previous studies [18,29] have hypothesized that the internal goethite layer (that layer close to the surface of the steel) contributed most heavily to the corrosion resistance of alloyed steels, thereby interfering with diffusion of chloride ions in the rust layer.

Based on the results from μXRD and SEM coupled with EDS presented herein, it can be hypothesized that this layer of goethite with Cr, found in the case of 16 wt.% Cr steel and absent in the case of 10 wt.% Cr steel, contributed to the decreased corrosion propagation of 16 wt.% Cr steel relative to that of 10 wt.% Cr steel, as shown by the impedance data (Tables 2 and 3). Since these Cr-substituted iron oxide-hydroxides were until now only found on synthesized iron oxide-hydroxides, further research has to be performed on other

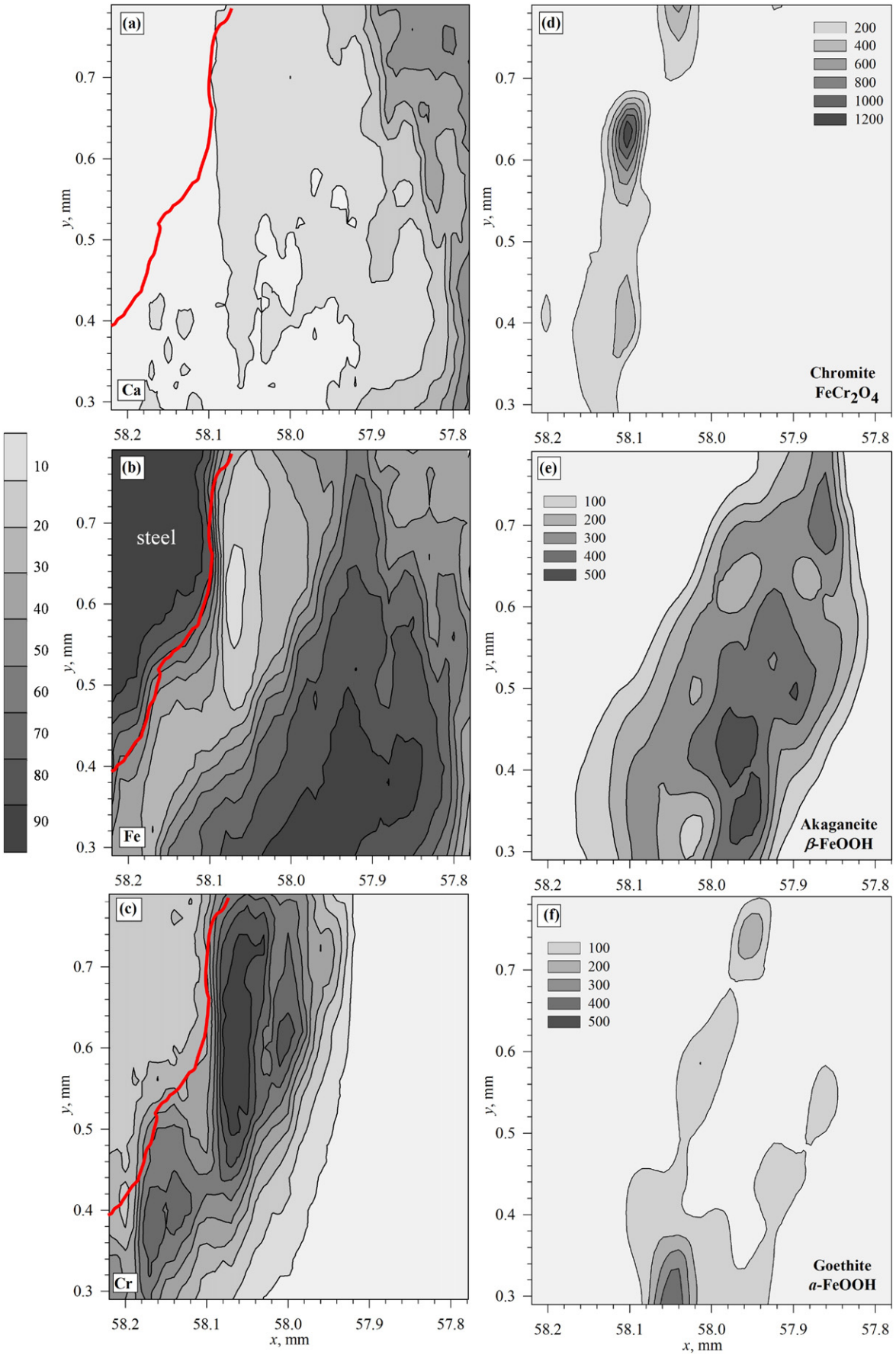

Fig. 9. 10 wt.% Cr steel reinforced mortar sample: μ-XRF elemental maps for (a) Ca, (b) Fe, and (c) Cr and corresponding intensity maps obtained through μ-XRD measurement showing distribution of (d) chromite ($FeCr_2O_4$), (e) akaganeite (β-FeOOH), and (f) goethite (α-FeOOH).

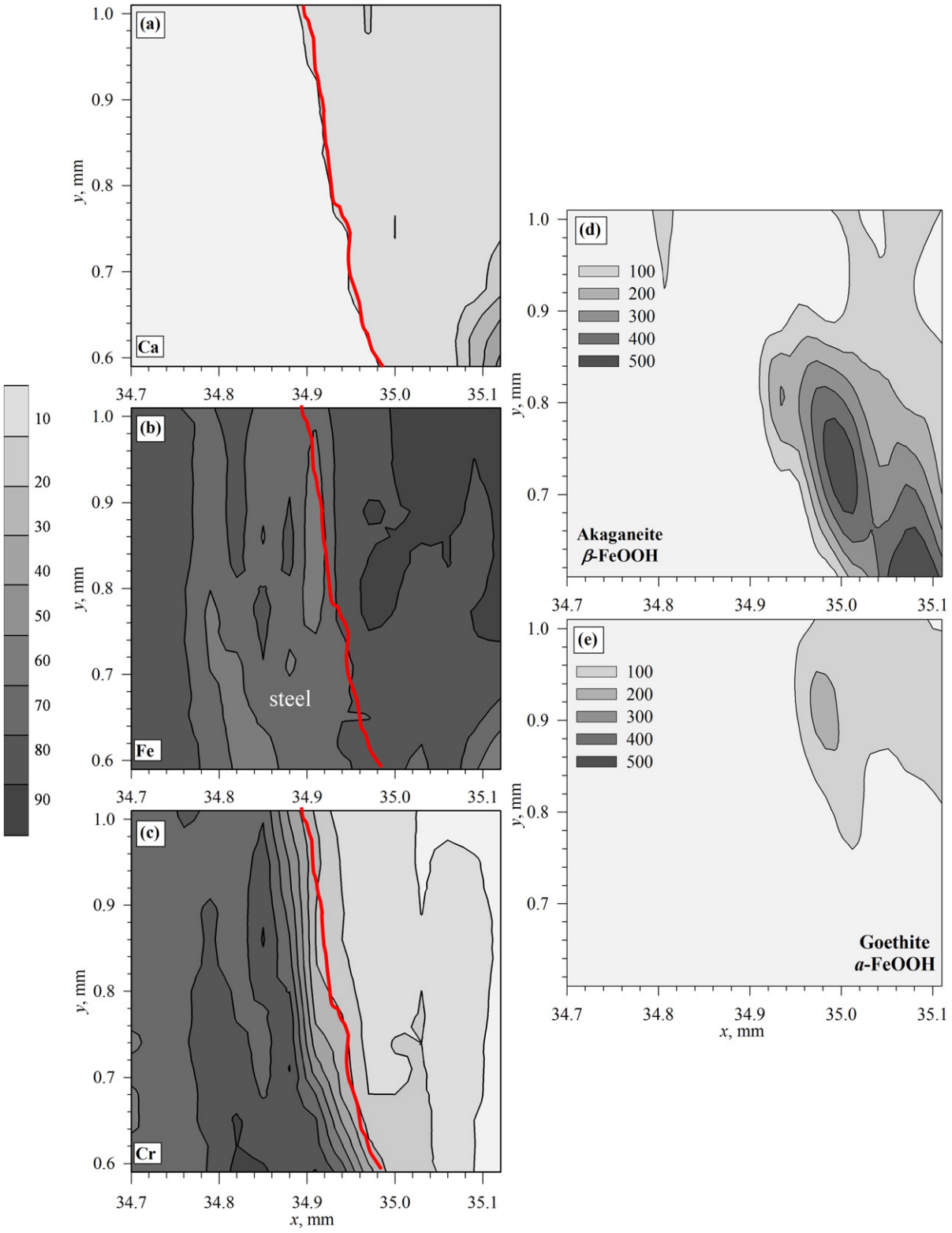

Fig. 10. 16 wt.% Cr steel reinforced mortar sample: μ-XRF elemental maps for (a) Ca, (b) Fe, and (c) Cr and corresponding intensity maps obtained through μ-XRD measurement showing distribution of (d) akaganeite (β-FeOOH), and (e) goethite (α-FeOOH).

reinforcing steel types with different Cr and Ni contents to confirm that such a substitution would occur naturally during corrosion of Cr alloyed steel in concrete under high pH and low oxygen availability. As earlier discussed, previous research on synthesized Cr-substituted iron oxide-hydroxides [18,28,30,31] have shown that the presence of Cr influences the size of the crystals. A similar behaviour could be expected in the case of corrosion products formed during corrosion of Cr-rich reinforcing steel in concrete. This would have a tremendous influence in concrete structures since any variation in crystallite formation, size, and morphology could potentially lead to differences in pressure at the steel/concrete interface, consequently influencing the onset of the cracking of concrete to occur.

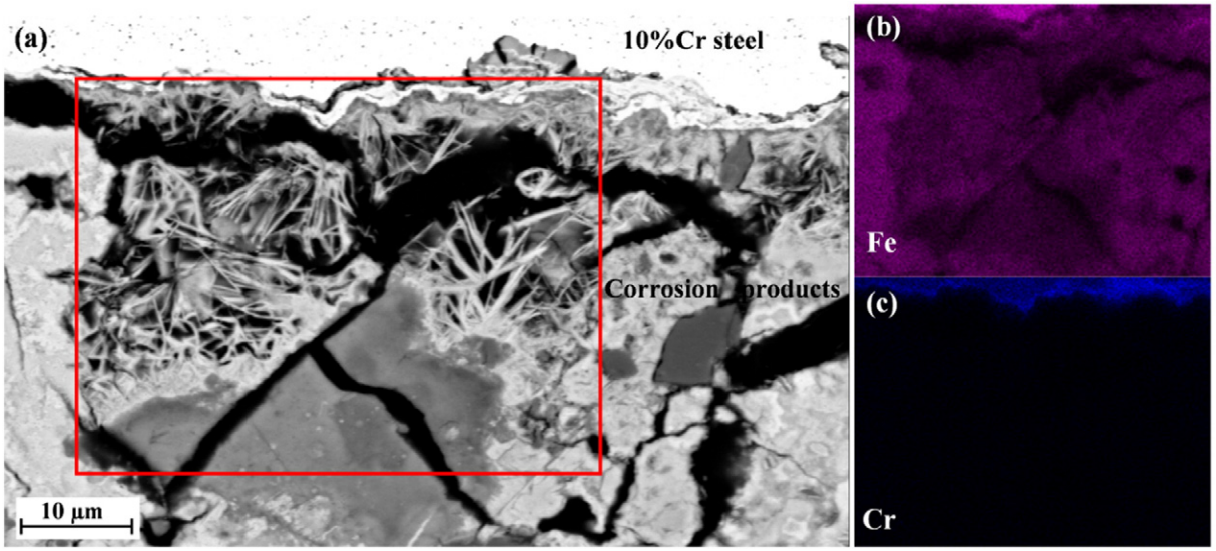

Fig. 11. An example of needle-like crystals mainly formed in voids and cracks around the surface of the 10 wt.% Cr steel, BSE image (a) with Fe (b) and Cr (c) distribution maps of the area indicated in the red box on (a), obtained by EDS.

4. Conclusions

Our results showed that scanning μ-XRD is a very useful tool for samples with nanocrystalline phases, enabling phase differentiation and 2-D distribution maps of corrosion products with high spatial resolution. Analysis of powder diffraction patterns revealed that the main phases formed during corrosion of two types of high-Cr, low-Ni corrosion resistant steels embedded in mortar were goethite and akageneite. Goethite is predominantly found closer to the surface of the steel and its growth is enhanced by the presence of chromium in the composition of reinforcing steel. Akageneite is found further away from the surface of the steel and its growth is attributed to the presence of chloride ions in the environment around the steel. In the case of steel with higher Cr content, corrosion products with Cr were identified using SEM and EDS.

Since the present work investigated a phenomenon only on a single set of samples, a follow up of the research would be to perform a statistical analysis to confirm reproducibility and repeatability of the applied experimental program.

Acknowledgements

This research was supported by scientific project "The composition of corrosion products on corrosion resistant concrete reinforcement" (Grant No. 73/10), funded by Unity through Knowledge Fund (UKF), and by scientific project "The Development of New Materials and Concrete Structure Protection Systems" (No. 082-0822161-2159), funded by Croatian Ministry of Education, Science and Sport. This publication was based on work supported in part by Award No. KUS-l1-004021, made by King Abdullah University of Science and Technology (KAUST). The Advanced Light Source is supported by the Director, Office of Science, Office of Basic Energy Sciences, of the U.S. Department of Energy under Contract No. DE-AC02-05CH11231.

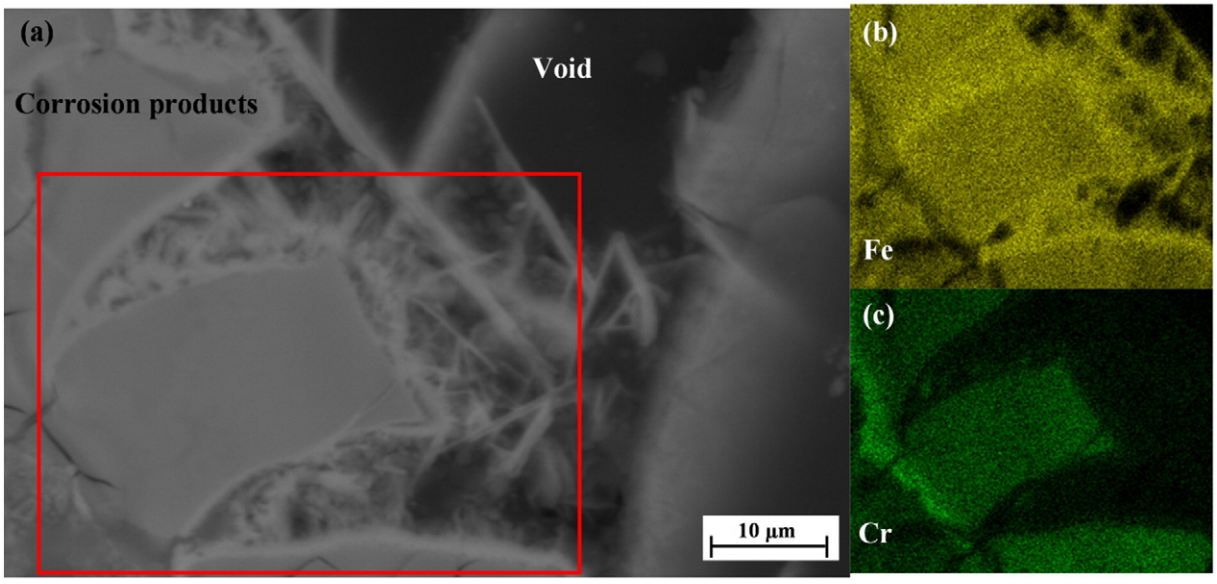

Fig. 12. An example of crystals mainly formed in voids in the cement matrix around the 16 wt.% Cr steel, BSE image (a) with Fe (b) and Cr (c) distribution maps of the area indicated in the red box on (a), obtained by EDS.

References

[1] P.K. Mehta, P.J. Monteiro, Concrete: Microstructure, Properties, and Materials, McGraw-Hill, New York, 2006.
[2] K. Tuutti, Corrosion of steel in concrete, Tech. Report, Swedish Cement and Concrete Research Institute, Stockholm, 1982.
[3] A. Bentur, S. Diamond, N. Berke, Steel Corrosion in Concrete, Fundamental and Civil Engineering Practice, E & FN Spoon, London, 1997.
[4] K. Bhargava, A.K. Ghosh, Y. Mori, S. Ramanujam, Modeling of time to corrosion-induced cover cracking in reinforced concrete structures, Cem. Concr. Res. 35 (2005) 2203–2218.
[5] T. Liu, R.W. Weyers, Modeling the dynamic corrosion process in chloride contaminated concrete structures, Cem. Concr. Res. 28 (1998) 365–379.
[6] S. Caré, Q.T. Nguyen, V. L'Hostis, Y. Berthaud, Mechanical properties of the rust layer induced by impressed current method in reinforced mortar, Cem. Concr. Res. 38 (2008) 1079–1091.
[7] H.S. Wong, Y.X. Zhao, A.R. Karimi, N.R. Buenfeld, W.L. Jin, On the penetration of corrosion products from reinforcing steel into concrete due to chloride-induced corrosion, Corros. Sci. 52 (2010) 2469–2480.
[8] A. Michel, B.J. Pease, M.R. Geiker, H. Stang, J.F. Olesen, Monitoring reinforcement corrosion and corrosion-induced cracking using non-destructive X-ray attenuation measurements, Cem. Concr. Res. 41 (2011) 1085–1094.
[9] Z.P. Bazant, Physical model for steel corrosion in concrete sea structures — application, J. Struct. Div. ASCE 105 (1979) 1155–1166.
[10] C.L. Page, K.W.J. Treadaway, Aspects of the electrochemistry of steel in concrete, Nature 297 (1982) 109–115.
[11] A.A. Torres-Acosta, A.A. Sagues, Concrete cracking by localized steel corrosion — geometric effects, ACI Mater. J. 101 (2004) 501–507.
[12] A. Raman, S. Nasrazadani, L. Sharma, Morphology of rust phases formed on weathering steels in various laboratory corrosion tests, Metallography 22 (1989) 79–96.
[13] D.A. Koleva, J. Hu, A.L.A. Fraaij, P. Stroeven, N. Boshkov, J.H.W. de Wit, Quantitative characterisation of steel/cement paste interface microstructure and corrosion phenomena in mortars suffering from chloride attack, Corros. Sci. 48 (2006) 4001–4019.
[14] R. Vera, M. Villarroel, A.M. Carvajal, E. Vera, C. Ortiz, Corrosion products of reinforcement in concrete in marine and industrial environments, Mater. Chem. Phys. 114 (2009) 467–474.
[15] J.J. Santana Rodríguez, F.J. Santana Hernández, J.E. González González, XRD and SEM studies of the layer of corrosion products for carbon steel in various different environments in the province of Las Palmas (The Canary Islands, Spain), Corros. Sci. 44 (2002) 2425–2438.
[16] D.A. Koleva, K. van Breugel, J.H.W. de Wit, E. van Westing, O. Copuroglu, L. Veleva, A.L.A. Fraaij, Correlation of microstructure, electrical properties and electrochemical phenomena in reinforced mortar. Breakdown to multi-phase interface structures. Part I: microstructural observations and electrical properties, Mater. Charact. 59 (2008) 290–300.
[17] D.A. Koleva, J.H.W. de Wit, K. van Breugel, L.P. Veleva, E. van Westing, O. Copuroglu, A.L.A. Fraaij, Correlation of microstructure, electrical properties and electrochemical phenomena in reinforced mortar. Breakdown to multi-phase interface structures. Part II: pore network, electrical properties and electrochemical response, Mater. Charact. 59 (2008) 801–815.
[18] D.C. Cook, S.J. Oh, R. Balasubramanian, M. Yamashita, The role of goethite in the formation of the protective corrosion layer on steels, Hyperfine Interact. 122 (1999) 59–70.
[19] F.R. Pérez, C.A. Barrero, O. Arnache, L.C. Sánchez, K.E. García, A.R. Hight Walker, Structural properties of iron phases formed on low alloy steels immersed in sodium chloride-rich solutions, Physica B 404 (2009) 1347–1353.
[20] R.D. Moser, P.M. Singh, L.F. Kahn, K.E. Kurtis, Chloride-induced corrosion resistance of high-strength stainless steels in simulated alkaline and carbonated concrete pore solutions, Corros. Sci. 57 (2012) 241–253.
[21] A. Bautista, G. Blanco, F. Velasco, A. Gutiérrez, L. Soriano, F.J. Palomares, H. Takenouti, Changes in the passive layer of corrugated austenitic stainless steel of low nickel content due to exposure to simulated pore solutions, Corros. Sci. 51 (2009) 785–792.
[22] H. Luo, C.F. Dong, X.G. Li, K. Xiao, The electrochemical behaviour of 2205 duplex stainless steel in alkaline solutions with different pH in the presence of chloride, Electrochim. Acta 64 (2012) 211–220.
[23] A. Bautista, A. González-Centeno, G. Blanco, S. Guzmán, Application of EIS to the study of corrosion behaviour of sintered ferritic stainless steels before and after high-temperature exposure, Mater. Charact. 59 (2008) 32–39.
[24] G. Blanco, A. Bautista, H. Takenouti, EIS study of passivation of austenitic and duplex stainless steels reinforcements in simulated pore solutions, Cem. Concr. Compos. 28 (2006) 212–219.
[25] M. Serdar, D. Bjegović, I. Stipanović Oslaković, Corrosion resistant steel reinforcement — laboratory and field testing, Proceeding of Concrete Under Severe Conditions Environment and Loading, Taylor & Francis Group, London, 2010.
[26] M.F. Hurley, J.R. Scully, Lateral and radial corrosion propagation behavior of 9–21% Cr and 18% Cr + 2.8% Mo stainless steel reinforcing materials in simulated concrete environments, Mater. Corros. 64 (2013) 752–763.
[27] C. Rémazeilles, Ph. Refait, On the formation of β-FeOOH (akaganéite) in chloride-containing environments, Corros. Sci. 49 (2007) 844–857.
[28] A.L. Morales, C.A. Barrero, F. Jaramillo, C. Arroyave, J.-M. Greneche, Properties of goethite grown under the presence of Cr^{3+}, Cu^{2+} and Mn^{2+} ions, Hyperfine Interact. 148–149 (2003).
[29] T. Ishikawa, R. Katoh, A. Yasukawa, K. Kandori, T. Nakayama, F. Yuse, Influences of metal ions on the formation of β-FeOOH particles, Corros. Sci. 43 (2001) 1727–1738.
[30] S. Krehula, S. Musić, The influence of a Cr-dopant on the properties of α-FeOOH particles precipitated in highly alkaline media, J. Alloys Compd. 469 (2009) 336–342.
[31] K.E. García, C.A. Barrero, A.L. Morales, J.M. Greneche, Characterization of akaganeite synthesized in presence of Al^{3+}, Cr^{3+}, and Cu^{2+} ions and urea, Mater. Chem. Phys. 112 (2008) 120–126.
[32] N. Tamura, M. Kunz, K. Chen, R.S. Celestre, A.A. MacDowell, T. Warwick, A superbend X-ray microdiffraction beamline at the advanced light source, Mater. Sci. Eng. A 524 (2009) 28–32.
[33] M. Kunz, N. Tamura, K. Chen, A.A. MacDowell, R.S. Celestre, M.M. Church, S. Fakra, E.E. Domning, J.M. Glossinger, J.L. Kirschman, G.Y. Morrison, D.W. Plate, B.V. Smith, T. Warwick, V.V. Yashchuk, H.A. Padmore, E. Ustundag, A dedicated superbend X-ray microdiffraction beamline for materials, geo-, and environmental sciences at the advanced light source, Rev. Sci. Instrum. 80 (2009).
[34] N. Tamura, A.A. MacDowell, R. Spolenak, B.C. Valek, J.C. Bravman, W.L. Brown, R.S. Celestre, H.A. Padmore, B.W. Batterman, J.R. Patel, Scanning X-ray microdiffraction with submicrometer white beam for strain/stress and orientation mapping in thin films, J. Synchrotron Radiat. 10 (2003) 137–143.
[35] A. Talekar, D. Chandra, R. Chellappa, J. Daemen, N. Tamura, M. Kunz, Oxidation kinetics of high strength low alloy steels at elevated temperatures, Corros. Sci. 50 (2008) 2804–2815.
[36] S. Omanovic, S.G. Roscoe, Interfacial behavior of β-lactoglobulin at a stainless steel surface: an electrochemical impedance spectroscopy study, J. Colloid Interface Sci. 227 (2000) 452–460.
[37] M. Farcas, N.P. Cosman, D.K. Ting, S.G. Roscoe, S. Omanovic, A comparative study of electrochemical techniques in investigating the adsorption behaviour of fibrinogen on platinum, J. Electroanal. Chem. 649 (2010) 206–218.
[38] L. Valek, S. Martinez, D. Mikulic, I. Brnardic, The inhibition activity of ascorbic acid towards corrosion of steel in alkaline media containing chloride ions, Corros. Sci. 50 (2008) 2705–2709.
[39] C. Andrade, M. Keddam, X.R. Nóvoa, M.C. Pérez, C.M. Rangel, H. Takenoutti, Electrochemical behaviour of steel rebars in concrete: influence of environmental factors and cement chemistry, Electrochim. Acta 46 (2001) 3905–3912.
[40] H. Yang, R. Lu, R.T. Downs, G. Costin, Goethite, α-FeO(OH), from single-crystal data, Acta Crystallogr. E 62 (2006) 250–252.
[41] J.E. Post, V.F. Buchwald, Crystal structure refinement of akaganeite, Am. Mineral. 76 (1991) 272–277.
[42] J.K. Kim, Y.H. Kim, J.S. Lee, K.Y. Kim, Effect of chromium content on intergranular corrosion and precipitation of Ti-stabilized ferritic stainless steels, Corros. Sci. 52 (2010) 1847–1852.
[43] J. Cai, J. Liu, Z. Gao, A. Navrotsky, S.L. Suib, Synthesis and anion exchange of tunnel structure akaganeite, Chem. Mater. 13 (2001) 4595–4602.